# Learning Event-guided Exposure-agnostic Video Frame Interpolation via Adaptive Feature Blending

Junsik Jung<sup>1</sup>
junsik.jung@kaist.ac.kr
Yoonki Cho<sup>1</sup>
ybonki@kaist.ac.kr
Woo Jae Kim<sup>1</sup>
wkim97@kaist.ac.kr
Lin Wang<sup>2</sup>
thwang@ntu.edu.sg
Sung-eui Yoon<sup>1</sup>
sungeui@kaist.edu

- School of Computing, Korea Advanced Institute of Science and Technology (KAIST), Daejeon, Korea
- <sup>2</sup> School of Electrical and Electronic Engineering, Nanyang Technological University (NTU), Singapore

#### Abstract

Exposure-agnostic video frame interpolation (VFI) is a challenging task that aims to recover sharp, high-frame-rate videos from blurry, low-frame-rate inputs captured under unknown and dynamic exposure conditions. Event cameras are sensors with high temporal resolution, making them especially advantageous for this task. However, existing event-guided methods struggle to produce satisfactory results on severely low-frame-rate blurry videos due to the lack of temporal constraints. In this paper, we introduce a novel event-guided framework for exposure-agnostic VFI, addressing this limitation through two key components: a Target-adaptive Event Sampling (TES) and a Target-adaptive Importance Mapping (TIM). Specifically, TES samples events around the target timestamp and the unknown exposure time to better align them with the corresponding blurry frames. TIM then generates an importance map that considers the temporal proximity and spatial relevance of consecutive features to the target. Guided by this map, our framework adaptively blends consecutive features, allowing temporally aligned features to serve as the primary cues while spatially relevant ones offer complementary support. Extensive experiments on both synthetic and real-world datasets demonstrate the effectiveness of our approach in exposure-agnostic VFI scenarios.

#### 1 Introduction

Video frame interpolation (VFI) aims to generate intermediate frames between consecutive inputs, converting low-frame-rate videos into high-frame-rate ones [2]. Recent advances in event cameras [3], which asynchronously capture per-pixel brightness changes with high temporal resolution, have significantly improved VFI performance [3, 23, 21], [21], [22], [23],

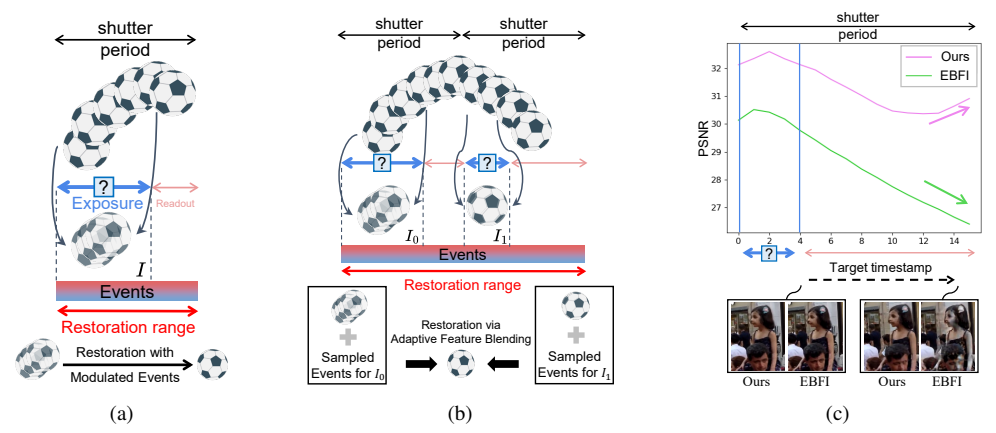


Figure 1: Schematic comparison with a prior event-guided exposure-agnostic VFI method. (a) EBFI [122] restores sharp frames from a single blurry input via event modulation, but degrades as the target timestamp deviates due to the lack of temporal constraints. (b) Our method addresses this by explicitly leveraging temporal constraints via adaptive feature blending. (c) PSNR comparison on GoPro [125] shows that our method maintains more stable performance across varying timestamps.

particularly in exposure-specific settings where the camera exposure time is fixed and known. However, in real-world scenarios, exposure time often varies and is blind due to auto-exposure mechanisms [2], resulting in inputs with inconsistent motion blur. This variability poses challenges for conventional VFI models, which are typically designed for either consistently sharp or blurry inputs. Consequently, there is a growing need for exposure-agnostic VFI, which can handle unknown and dynamic exposure conditions and is thus essential for practicality.

Recently, a few event-guided methods [15], [27] have been proposed for exposure-agnostic video restoration. UEVD [15] introduced an event-guided method for video deblurring under blind exposure conditions. However, it is limited to restoring a single sharp frame within the exposure window corresponding to the blurry input, and requires a separate VFI step to generate high-frame-rate outputs. EBFI [12] later proposed a unified framework that restores arbitrary target frames under blind exposure from a single blurry frame by modulating events (see Fig. 1(a)). Yet, the lack of temporal constraints — that is, leveraging the temporal relationships between neighboring frames for consistent and accurate guidance — leads to performance degradation, especially when input videos are captured at very low frame rates.

To address this limitation, a promising direction is to introduce *temporal constraints* across consecutive frames since frames closer to the target timestamp often offer more relevant cues. Flow-based methods [1], [1], [1], [1]] offer a natural way to model such constraints by aligning frame-to-frame correspondences. However, their effectiveness is limited under blind exposure, where severe motion blur degrades both frame quality and flow estimation [1]. An alternative is to leverage the *mutual relationship* between frames and events [1], which introduces two key challenges: (1) how to sample events between the target timestamp and the unknown exposure period in a way that reflects the mutual relationship between frames and events, and (2) how to impose temporal constraints across consecutive features while jointly considering temporal proximity and spatial relevance.

In this paper, we address the aforementioned challenges through a simple yet effective adaptive feature blending strategy (see Fig. 1(b)). To this end, we introduce a novel learning

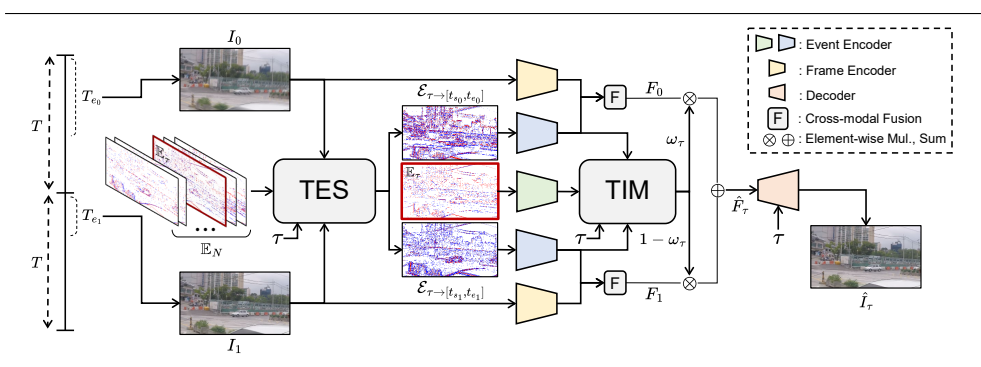


Figure 2: Overview of our framework. Given blurry frames  $(I_0, I_1)$  with unknown exposures  $(T_{e_0}, T_{e_1})$ , stacked events  $\mathbb{E}_N$  over 2T, and target timestamp  $\tau$ , the model reconstructs the target frame  $\hat{I}_{\tau}$ . TES samples events around  $\tau$  and unknown exposure, which are fused with frames. TIM generates an importance map  $\omega_{\tau}$  to adaptively blend the fused features  $(F_0, F_1)$  into  $F_{\tau}$ , which is then decoded into  $\hat{I}_{\tau}$ . Shared encoders are color-coded.

framework that consists of two key modules: the Target-adaptive Event Sampling (TES) and the Target-adaptive Importance Mapping (TIM). TES samples events around the target timestamp and the unknown exposure period, which are fused with the corresponding blurry frames to guide target sharp frame synthesis. TIM is designed to generate an importance map that adaptively weights features from consecutive frames based on their temporal proximity and spatial relevance to the target. This allows our model to incorporate temporal constraints and maintain performance even as the target timestamp deviates (see Fig.1(c)). Experiments on synthetic and real-world datasets show that our method consistently outperforms existing approaches under blind exposure, achieving at least a 2dB PSNR improvement.

In summary, our contributions are threefold: 1) We propose a simple yet effective feature blending strategy that, for the first time, incorporates temporal constraints into event-guided VFI under unknown and dynamic exposure conditions. 2) We design a novel unified framework with two synergistic modules: TES, which samples events around the target timestamp and unknown exposure; and TIM, which generates an importance map to adaptively weight features based on temporal and spatial relevance. 3) We validate our approach through extensive experiments on synthetic and real-world datasets, showing its effectiveness across diverse blind exposure scenarios.

#### 2 Related Work

Exposure-specific Video Restoration. Most prior work assumes a known and fixed exposure time when restoring sharp, high-frame-rate videos. For video frame interpolation (VFI), existing methods are broadly categorized into flow-based [II, III, III, III, III], kernel-based [III, III], architecture-based [III, III], and event-guided [III, III], IIII] approaches. Motion deblurring has also been studied independently to restore one sharp frame from each blurry input [II, III], III], III]. Rather than treating VFI and motion deblurring as separate tasks, recent studies have explored unified frameworks that address both jointly, using either RGB-only [III], III] or event-guided settings [III], III]. However, their reliance on fixed exposure limits their applicability to real-world scenarios where exposure is unknown and dynamically changing.

Exposure-agnostic Video Restoration. A few RGB-only methods [44] have been pro-

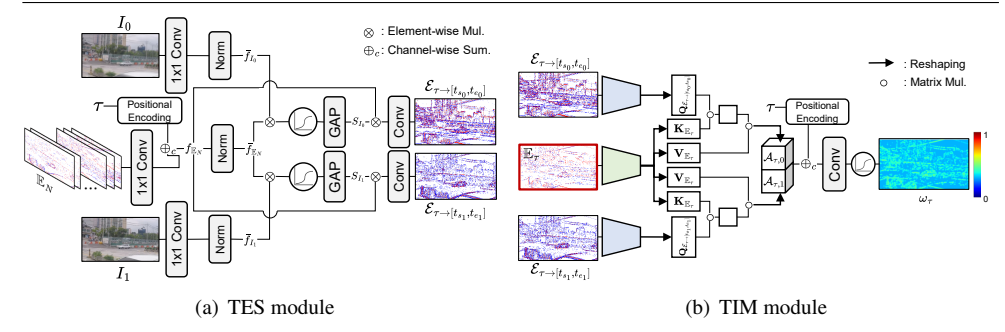


Figure 3: Architectures of the TES (Sec. 3.2) and TIM (Sec. 3.3) modules.

posed for video restoration under unknown exposure conditions. However, due to the lack of precise motion cues, these approaches suffer from motion ambiguity [11], [12], making it difficult to accurately recover sharp frames. To overcome this, event cameras offer a promising alternative by providing temporally dense and precise motion information. Building on this idea, Kim *et al.* [15] proposed an event-guided motion deblurring method under blind exposure. However, their approach is limited to reconstructing a single sharp frame within the exposure window and requires an additional VFI step to generate high-frame-rate output. Weng *et al.* [12] presented a framework for interpolating arbitrary frames by modulating a blurry frame with events, but the lack of temporal constraints leads to degraded performance under severe blur and sparse temporal sampling. We address this limitation with a unified framework that explicitly incorporates temporal constraints into event-guided, exposure-agnostic VFI.

#### 3 Method

In this section, we first formulate the problem based on the mutual relationship between frames and events using the Event-based Double Integral (EDI) model [23]. We then present an overview of our framework (Sec.3.1), followed by details of the proposed TES and TIM modules (Sec.3.2, 3.3).

**Problem Formulation.** Event cameras capture events, denoted as  $e(\mathcal{T})$ , at timestamp  $\mathcal{T}$  across the pixel space asynchronously  $[\mathbf{B}]$ . These events are recorded when the logarithmic change in intensity exceeds a contrast threshold c. During the exposure time  $T_e$ , the captured frame I is derived by averaging latent frames L(t) present in  $T_e$  as:

$$I = \frac{1}{T_e} \int_{t_s}^{t_e} L(t)dt, \tag{1}$$

where L,  $t_s$ , and  $t_e$  denote the latent frame, the starting timestamp of  $T_e$ , and the end timestamp of  $T_e$ , respectively.

Given latent frames  $L(\tau)$  and L(t) at different timestamps  $\tau$  and t during the exposure time, and the events spanning the interval  $[\tau, t]$ , we can establish the following relationship between the latent frames:

$$L(t) = L(\tau) \exp\left(c \cdot \mathcal{E}_{\tau \to t}\right),\tag{2}$$

where  $\mathcal{E}_{\tau \to t} = \int_{\tau}^{t} e(x) dx$  denotes a 2D tensor obtained by stacking events from  $\tau$  to t. Combining Eqs. (1) and (2), the following Event-based Double Integral (EDI) model [ $\square$ ] can be derived:

$$L(\tau) = \frac{T_e \cdot I}{\int_{t_-}^{t_e} \exp(c \cdot \mathcal{E}_{\tau \to t}) dt}.$$
 (3)

The EDI model describes how the latent frame  $L(\tau)$  can be reconstructed by combining the captured frame I with stacked events over the exposure duration  $T_e$ . In VFI scenarios where the target timestamp  $\tau$  lies beyond  $T_e$ , EVDI [ $\square$ ] extended such mutual relationship by using events from  $\tau$  to  $T_e$  to restore sharp frames outside the exposure window. However, this approach requires precise knowledge of  $T_e$ , limiting its practicality. Nonetheless, this suggests that if we can approximate events centered around  $\tau$  and  $T_e$  without knowing  $T_e$ , it is still possible to recover  $L(\tau)$  based on Eq. (3). We denote this event set as  $\mathcal{E}_{\tau \to [t_s, t_e]}$ .

#### 3.1 Overview

We adopt a UNet-based encoder-decoder model [2], comprising three encoders and two decoders, with a refinement block [2] appended at the final decoder stage. The model takes as input two consecutive captured frames  $(I_0,I_1)$  — each recorded under unknown exposure durations  $(T_{e_0},T_{e_1})$  — along with the corresponding events recorded during their shutter periods 2T. These events are converted into event frames [2] by pixel-wise accumulation over N bins, yielding  $\mathbb{E}_N \in \mathbb{R}^{N \times H \times W}$ , where N denotes the number of temporal slices.

To apply Eq. (3), we sample a subset of events  $\mathcal{E}_{\tau \to [t_s, t_e]}$  from the stacked input  $\mathbb{E}_N$ , centered around the target timestamp  $\tau$  and unknown exposure  $T_e$ . To this end, we introduce the Target-adaptive Event Sampling (TES) module (Sec. 3.2), samples  $(\mathcal{E}_{\tau \to [t_{s_0}, t_{e_0}]}, \mathcal{E}_{\tau \to [t_{s_1}, t_{e_1}]})$  accordingly. Frame and event features from  $(I_0, I_1)$  and sampled events are fused via a cross-modal technique [59] to produce  $(F_0, F_1)$ .

To leverage temporal constraints, we introduce the Target-adaptive Importance Mapping (TIM) module (Sec. 3.3), which generates an importance map  $\omega_{\tau}$  based on the temporal proximity and spatial relevance of  $(F_0, F_1)$  to  $\tau$ . This map guides adaptive blending: temporally closer features are emphasized, while spatially relevant cues complement them. The resulting fused feature  $\hat{F}_{\tau}$  is decoded to reconstruct the target frame  $\hat{I}_{\tau}$ .

## 3.2 Target-adaptive Event Sampling

Recalling Eq. (3), the frames  $(I_0, I_1)$  should be combined with events centered around the target timestamp  $\tau$  and the unknown exposure durations  $(T_{e_0}, T_{e_1})$ . To achieve this, we follow prior methods [17] by using the captured frames as references under blind exposure. However, unlike previous approaches that focus solely on the unknown exposure period, our module is additionally designed to account for the target timestamp  $\tau$ .

A detailed illustration of the TES module is shown in Fig. 3(a). For clarity, we describe the process of sampling the stacked events for  $I_0$ , denoted as  $\mathcal{E}_{\tau \to [t_{s_0}, t_{e_0}]}$ . Given  $\mathbb{E}_N$ ,  $I_0$ , and  $\tau$  as inputs, the TES module is formulated as:

$$\mathcal{E}_{\tau \to [t_{s_0}, t_{e_0}]} = \text{TES}(\mathbb{E}_N, I_0, \tau). \tag{4}$$

We first extract features from  $\mathbb{E}_N$  and  $I_0$ . To incorporate the target timestamp  $\tau$ , we add its positional encoding to the event features channel-wise, yielding  $f_{\mathbb{E}_N}$ . We then compute the correlation score  $\mathcal{S}_{I_0}$  between the normalized features of  $\bar{f}_{I_0}$  and  $\bar{f}_{\mathbb{E}_N}$  as:

$$S_{I_0} = GAP(\sigma(\bar{f}_{I_0} \otimes \bar{f}_{\mathbb{E}_N})), \tag{5}$$

where  $\otimes$ ,  $\sigma$ , and GAP denote element-wise multiplication, the sigmoid function, and global average pooling, respectively. Using  $\mathcal{S}_{I_0}$ , we perform element-wise multiplication with  $f_{\mathbb{E}_N}$  to sample the event features centered around  $\tau$  and  $T_{e_0}$ . A convolution is then applied to produce the final representation  $\mathcal{E}_{\tau \to [t_{s_0},t_{e_0}]}$ . The counterpart  $\mathcal{E}_{\tau \to [t_{s_1},t_{e_1}]}$  is derived analogously using  $I_1$ , and both event representations are fused with  $(I_0,I_1)$  using the fusion method from [59] (denoted as 'F' in Fig. 2).

Table 1: Summary of compared methods. 'Frame' and 'Events' denote input types; 'Agnostic' and 'Unified' indicate support for blind exposure and joint deblurring-interpolation; 'T-Constraint' refers to the use of temporal constraints.

Method	Frame	Events	Agnostic	Unified	T-Constraint
NAFNet [1]+RIFE [1]	/	Х	Х	Х	✓(via RIFE)
UTI 🔤]	/	×	✓	/	✓
VIDUE [☑]	/	×	✓	/	✓
UEVD [□]+TL [□]	/	✓	√(via UEVD)	×	✓(via TL)
EVDI 🗖	/	1	X	1	✓
REFID [	/	✓	X	/	✓
EBFI [	/	✓	✓	/	X
Ours	✓	✓	✓	✓	✓

## 3.3 Target-adaptive Importance Mapping

Although TES provides relevant events, restoration degrades as  $\tau$  shifts from the exposure due to event sensor noise [ $\square$ ]. When  $\tau$  nears  $T_{e_1}$ , relying only on  $I_0$  becomes suboptimal, making features from  $I_1$  more informative and underscoring the need for temporal constraints.

To address this, we introduce the TIM module, which estimates an importance map  $\omega_{\tau}$  to adaptively weight fused features  $(F_0, F_1)$  based on their temporal proximity and spatial relevance to the target. Given the sampled events  $(\mathcal{E}_{\tau \to [t_{s_0}, t_{e_0}]}, \mathcal{E}_{\tau \to [t_{s_1}, t_{e_1}]})$ , the  $\tau$ -centered event stack  $\mathbb{E}_{\tau}$ , and the timestamp  $\tau$ , TIM estimates  $\omega_{\tau}$  as:

$$\boldsymbol{\omega}_{\tau} = \text{TIM}(\mathcal{E}_{\tau \to [t_{s_0}, t_{e_0}]}, \mathcal{E}_{\tau \to [t_{s_1}, t_{e_1}]}, \mathbb{E}_{\tau}, \tau). \tag{6}$$

A detailed illustration of the TIM module is shown in Fig.3(b). We first extract features from the sampled events  $(\mathcal{E}_{\tau \to [t_{s_0},t_{e_0}]},\mathcal{E}_{\tau \to [t_{s_1},t_{e_1}]})$  and the  $\tau$ -centered event stack  $\mathbb{E}_{\tau}$ . To estimate spatial relevance efficiently, we apply channel-wise attention [ $\mathbb{E}_{\tau}$ ]: features from the sampled events are used as queries, and those from  $\mathbb{E}_{\tau}$  serve as keys and values. After flattening the spatial dimensions, the attended feature  $\mathcal{A}_{\tau,0}$  is computed as:

$$\mathcal{A}_{\tau,0} = \mathbf{V}_{\mathbb{E}_{\tau}} \circ \operatorname{softmax} \left( \frac{\mathbf{Q}_{\mathcal{E}_{\tau \to [t_{s_0}, t_{e_0}]}}^T \circ \mathbf{K}_{\mathbb{E}_{\tau}}}{\sqrt{d_k}} \right), \tag{7}$$

where  $d_k$  denotes the key dimension.  $\mathcal{A}_{\tau,1}$  is computed analogously. The two attended features are concatenated and combined with the positional encoding of  $\tau$  via channel-wise addition to encode temporal information. The result is passed through convolutional layers and a sigmoid activation to produce the importance map  $\omega_{\tau}$ , which encodes both temporal proximity and spatial relevance.

The target feature  $\hat{F}_{\tau}$  is obtained via an adaptive blending strategy that applies temporal constraints:

$$\hat{F}_{\tau} = (\boldsymbol{\omega}_{\tau} \otimes F_0) \oplus ((1 - \boldsymbol{\omega}_{\tau}) \otimes F_1). \tag{8}$$

A decoder then transforms  $\hat{F}_{\tau}$  into the target sharp frame  $\hat{I}_{\tau}$ . This blending strategy enables the model to effectively leverage temporal constraints between consecutive features. The entire framework is trained end-to-end using the Charbonnier loss [ $\square$ ]:

$$\mathcal{L} = \sqrt{\|I_{\tau}^{gt} - \hat{I}_{\tau}\|^2 + \varepsilon^2}, \text{with } \varepsilon = 1e-6.$$
 (9)

# 4 Experiments

#### 4.1 Experimental Setups

**Datasets.** We evaluate on GoPro [26] (with synthetic events from ESIM [50]), HighREV [40] (real events,  $1632 \times 1224$ ), and RealBlur-DAVIS [42] (real blurry videos and events). To

Table 2: Quantitative results on GoPro and HighREV ( $10\Downarrow$ ). **Bold** and <u>underlined</u> indicate the best and second-best scores, respectively.

Method	PSNR ↑ / SSIM ↑ / LPIPS ↓									
GoPro-10↓	9+1	5+5	1+9	RandEx						
NAFnet [□]+RIFE [□]	23.15 / 0.736 / 0.164	21.82 / 0.665 / 0.188	18.78 / 0.520 / 0.282	21.05 / 0.633 / 0.219						
UTI 🔤]	23.84 / 0.805 / 0.205	23.25 / 0.771 / 0.166	20.95 / 0.640 /0.170	22.17 / 0.714 / 0.189						
VIDUE [🚾]	25.37 / 0.818 / 0.181	26.24 / 0.835 / 0.145	24.76 / 0.764 / 0.146	25.86 / 0.819 / 0.152						
UEVD [🍱]+TL [🛄]	23.40 / 0.720 / 0.194	23.31 / 0.755 / 0.161	26.33 / 0.866 / 0.103	23.51 / 0.757 / 0.164						
EVDI 🛄	28.18 / 0.898 / <u>0.052</u>	27.73 / 0.884 / <u>0.067</u>	26.07 / 0.834 / 0.084	27.51 / 0.877 / <u>0.071</u>						
REFID [III]	31.08 / 0.939 / 0.077	31.28 / 0.941 / 0.071	30.27 / <u>0.927</u> / <u>0.078</u>	31.03 / 0.938 / 0.074						
EBFI 🚾]	31.06 / <u>0.942</u> / 0.072	31.08 / 0.940 / 0.071	30.32 / 0.921 / 0.087	30.89 / 0.936 / 0.075						
Ours	33.22 / 0.960 / 0.050	33.61 / 0.963 / 0.042	32.87 / 0.954 / 0.048	33.39 / 0.961 / 0.045						
HighREV-10↓										
NAFnet [□]+RIFE [□]	25.09 / 0.805 / 0.446	24.90 / 0.874 / 0.401	26.07 / 0.897 / 0.361	25.20 / 0.844 / 0.402						
UTI 🏧	26.22 / 0.834 / 0.371	26.15 / 0.821 / 0.395	26.51 / 0.851 / 0.395	26.19 / 0.831 / 0.398						
VIDUE [₩]	26.65 / 0.847 / 0.375	27.43 / 0.860 / 0.367	25.31 / 0.841 / 0.387	26.76 / 0.850 / 0.373						
UEVD [🗂]+TL 🛄	26.02 /0.844 / 0.399	27.41 / 0.854 / 0.378	27.77 / 0.861 / 0.337	27.43 / 0.854 / 0.373						
EVDI 🛄	30.26 / 0.910 / <u>0.278</u>	29.75 / 0.896 / <u>0.277</u>	27.01 / 0.839 / 0.292	29.25 / 0.887 / <u>0.273</u>						
REFID [🛄]	33.60 / 0.937 / 0.306	34.18 / 0.938 / 0.296	33.38 / 0.928 / 0.260	33.91 / 0.936 / 0.292						
EBFI 🚾]	28.23 / 0.898 / 0.362	27.84 / 0.887 / 0.342	26.25 / 0.855 / 0.279	27.55 / 0.882 / 0.333						
Ours	35.73 / 0.948 / 0.263	36.27 / 0.949 / 0.250	35.45 / 0.942 / 0.248	36.02 / 0.947 / 0.253						

Table 3: Quantitative results on GoPro and HighREV ( $16 \Downarrow$ ).

Method		PS	NR ↑ / SSIM ↑ / LPIP	S↓	
GoPro-16↓	15+1	11+5	5+11	1+15	RandEx
NAFnet [□]+RIFE [□]	21.37 / 0.645 / 0.297	21.10 / 0.627 / 0.284	19.75 / 0.551 / 0.270	17.32 / 0.430 / 0.322	20.03 / 0.569 / 0.233
UTI 🔤	21.43 / 0.672 / 0.286	21.19 / 0.659 / 0.273	20.23 / 0.591 / 0.272	19.64 / 0.534 / 0.298	20.74 / 0.609 / 0.234
VIDUE [☑]	22.44 / 0.686 / 0.298	23.27 / 0.721 / 0.270	23.10 / 0.697 / 0.231	21.58 / 0.623 / 0.220	22.89 / 0.695 / 0.253
UEVD [11]+TL [11]	17.04 / 0.316 / 0.472	17.26 / 0.334 / 0.459	17.92 / 0.376 / 0.444	18.41 / 0.401 / 0.438	17.64 / 0.357 / 0.453
EVDI [🗖]	27.38 / 0.881 / 0.083	27.16 / 0.874 / <u>0.084</u>	26.36 / 0.847 / <u>0.092</u>	24.15 / 0.774 / <u>0.115</u>	26.52 / 0.853 / <u>0.088</u>
REFID [III]	28.98 / 0.912 / 0.118	29.11 / 0.913 / 0.115	28.84 / 0.909 / 0.115	28.16 / 0.896 / 0.123	28.87 / 0.909 / 0.116
EBFI [	28.78 / <u>0.913</u> / 0.108	28.92 / <u>0.914</u> / 0.106	28.48 / 0.903 / 0.116	27.64 / 0.883 / 0.134	28.59 / 0.906 / 0.113
Ours	30.97 / 0.937 / 0.081	31.39 / 0.941 / 0.074	31.18 / 0.938 / 0.075	30.07 / 0.925 / 0.085	31.14 / 0.938 / 0.076
HighREV-16↓					
NAFnet [1]+RIFE [1]	19.85 / 0.336 / 0.744	19.70 / 0.285 / 0.770	19.91 / 0.312 / 0.764	20.35 / 0.332 / 0.734	19.53 / 0.287 / 0.765
UTI 🚾]	21.02 / 0.333 / 0.717	21.83 / 0.369 / 0.685	20.68 / 0.350 / 0.756	20.74 / 0.359 / 0.743	21.16 / 0.347 / 0.712
VIDUE [🚾]	21.63 / 0.356 / 0.721	21.82 / 0.364 / 0.718	21.63 / 0.370 / 0.713	21.21 / 0.372 / 0.704	21.64 / 0.366 / 0.715
UEVD [🗖]+TL 🛅	24.26 / 0.813 / 0.433	24.94 / 0.818 / 0.425	26.13 / 0.827 / 0.407	26.92 / 0.828 / 0.379	25.58 / 0.822 / 0.414
EVDI [🗖]	28.75 / 0.893 / <u>0.324</u>	28.62 / 0.887 / <u>0.323</u>	27.09 / 0.870 / <u>0.339</u>	24.16 / 0.786 / 0.386	27.33 / 0.875 / <u>0.336</u>
REFID [	30.51 / 0.921 / 0.349	30.91 / 0.922 / 0.346	30.68 / 0.918 / 0.346	29.59 / 0.907 / 0.342	30.60 / 0.919 / 0.346
EBFI [	26.28 / 0.883 / 0.380	26.18 / 0.878 / 0.37	25.24 / 0.860 / 0.350	23.95 / 0.829 / 0.382	25.54 / 0.866 / 0.355
Ours	33.36 / 0.937 / 0.312	33.93 / 0.938 / 0.307	33.85 / 0.937 / 0.303	32.70 / 0.929 / 0.282	33.69 / 0.937 / 0.303

simulate motion blur in GoPro and HighREV, we average m consecutive frames within the exposure duration and downsample them to shutter periods of 10 and 16 frames, denoted as  $10 \Downarrow$  and  $16 \Downarrow$ .

**Implementation Details.** Our framework is trained end-to-end without pre-training. We train on GoPro for 300 epochs using AdamW [21] with a learning rate of 5e-4, scheduled by cosine annealing [21], and fine-tune on HighREV for 20 epochs with a learning rate of 1e-4. We follow the official data splits. During training, m is randomly sampled within the shutter period (e.g.,  $m \in [1,9]$  for  $10 \Downarrow$ ), and inputs are cropped to  $128 \times 128$  (GoPro) or  $256 \times 256$  (HighREV). Target timestamps are randomly selected from available indices.

**Evaluation Protocols.** We evaluate under two settings: (1) *Symmetric exposure* with fixed m values ([1,5,9] for  $10 \Downarrow$ , [1,5,11,15] for  $16 \Downarrow$ ), and (2) RandEx, where m is randomly sampled as in training. Metrics include PSNR (dB), SSIM [13], and LPIPS [14]. We additionally report temporal consistency metrics (tOF, tLP [13]) and NIQE [13] for RealBlur-DAVIS, which lacks ground-truth frames.

#### 4.2 Comparison to the State-of-the-arts

Table 1 shows the summary of each compared method. All methods are retrained for fair comparison, except TimeLens (TL), which is evaluated using its pre-trained model due to unavailable training code. Exposure-specific baselines are provided with ground-truth exposure information. All results are averaged across the restored frames.

Quantitative Evaluation. Tables 2 and 3 show results on GoPro and HighREV under 10\$\\$

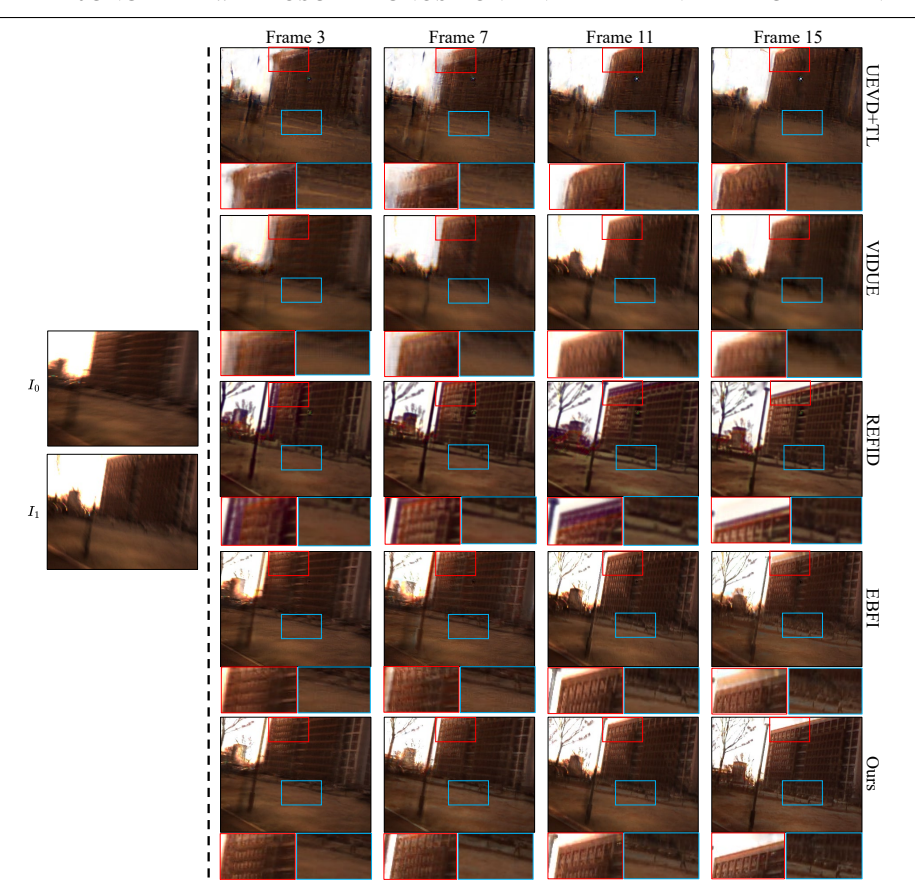


Figure 4: Qualitative results on RealBlur-DAVIS (real blur & events)

and 16\$\psi\$ settings. As expected, RGB-only and cascaded methods tend to yield lower performance, likely due to motion ambiguity and error propagation, respectively. Exposure-specific models (REFID, EVDI), trained with known exposure times, benefit from temporal alignment and produce comparable results. EBFI, despite being exposure-agnostic, performs competitively on GoPro, but its performance declines on HighREV, where larger pixel displacement highlights the importance of temporal constraints. Our method achieves the highest PSNR, SSIM, and LPIPS on both GoPro and HighREV, with margins up to 2.85dB over the second-best. Temporal consistency (tOF, tLP) and NIQE results on RealBlur-DAVIS are provided in the supplementary material (Sec. A.1).

**Qualitative Evaluation.** We present qualitative results on RealBlur-DAVIS (real captured video) in Fig. 4, where our method produces temporally consistent frames with minimal artifacts. Additional comparisons on GoPro, HighREV (with synthetic events), and RealBlur-DAVIS, along with supplementary video clips demonstrating qualitative results and arbitrary temporal upscaling, are provided in supplementary material (Sec. A.2).

#### 4.3 Analysis

**Analysis of the TES Module.** We analyze whether TES effectively samples events around the target timestamp  $\tau$  and the unknown exposure  $T_e$ . To this end, we apply a gradient-based interpretation [ $\square$ ] and compute importance scores as  $\frac{\partial \mathcal{E}_{\tau \to T_e}}{\partial \mathbb{E}_N}$ , indicating the contribution of each event to the sampled output. Given that input events are divided into N temporal bins

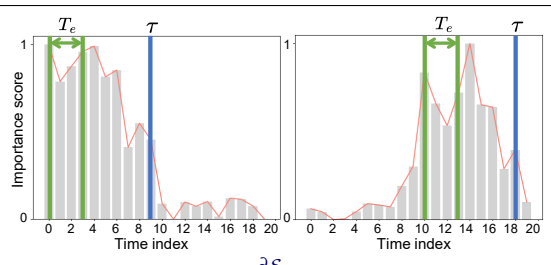


Figure 5: Channel-wise importance score  $\frac{\partial \mathcal{E}_{\tau \to [r_s, t_e]}}{\partial \mathbb{E}_N}$  indicating the sampling contribution of each time index. TES effectively selects events near the unknown exposure  $T_e$  (green) and target timestamp  $\tau$  (blue), regardless of whether  $\tau$  lies outside the exposure window.

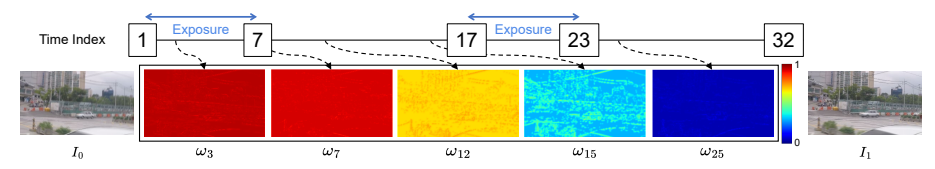


Figure 6: Visualization of importance maps  $\omega_{\tau}$  for  $\tau \in 3, 7, 12, 15, 25$ , with symmetric exposure durations (m = 7) for  $I_0$  and  $I_1$ .

and stacked channel-wise, we report the average importance score per channel on GoPro-10 $\psi$ . As shown in Fig. 5, TES consistently focuses on events near both  $T_e$  and  $\tau$ , even when  $\tau$  lies outside the exposure window.

We present ablation results on GoPro- $10\downarrow$  (RandEx) in the 'TES' section of Table 4. We evaluate the impact of removing key components from the TES module: (1) the sampling process in Eq. (5) and (2) the positional encoding (PE) of the target timestamp  $\tau$ . Removing the sampling process hinders the TES module from focusing on events near  $\tau$  and the blind exposure  $T_e$ , while excluding PE causes the module to ignore  $\tau$  and focus only on  $T_e$ . These degradations confirm that both components are essential for effective event sampling. Further qualitative ablations are included in the supplementary (Sec. A.3).

Analysis of the TIM Module. We visualize the importance map  $\omega_{\tau}$  in Fig. 6 using GoPro-16\$\psi\$ data with m=7, where the exposure ranges are [1,7] for  $I_0$  and [17,23] for  $I_1$ . As  $\tau$  approaches the exposure of  $I_0$ ,  $\omega_{\tau}$  assigns greater weights to features from  $I_0$ , and likewise shifts toward  $I_1$  as  $\tau$  nears its exposure. These results show that TIM adaptively emphasizes features that are temporally closer and spatially relevant to the target timestamp.

are provided in the supplementary (Sec. A.3).

Table 4: Ablation study on GoPro-10 $\downarrow$  (RandEx). All ablations are retrained from scratch, except Swap  $\omega_{\tau}$ .

Ablation	PSNR ↑	SSIM ↑	LPIPS ↓
TES (Fig. 3(a))			
Remove Sampling	32.05	0.948	0.058
Remove τ	31.12	0.937	0.073
TIM (Fig. 3(b))			
Remove τ		×	
Remove Eq. 7	32.24	0.945	0.051
Fixed $\omega_{\tau} = 0.5$	31.51	0.939	0.068
Swap $\omega_{\tau}$	20.43	0.588	0.194
Ours	33.39	0.961	0.045

We report ablation results for the TIM module in the 'TIM' section of Table 4. Removing the target timestamp  $\tau$  causes convergence failure, underscoring its importance for generating  $\omega_{\tau}$ . Disabling the attention mechanism in Eq. 7 also degrades performance, confirming the benefit of spatial relevance. We also evaluate two variants: replacing  $\omega_{\tau}$  with a constant value (0.5) and swapping its order during feature blending in Eq. (8). Both degrade performance, with the swapped version performing notably worse, validating the importance and learned structure of  $\omega_{\tau}$ . Qualitative ablations

#### 5 Conclusion

In this work, we proposed a simple yet effective framework for event-guided, exposure-agnostic video frame interpolation that explicitly incorporates temporal constraints via adaptive feature blending. Our method integrates two synergistic modules: the Target-adaptive Event Sampling module for event sampling around the target timestamp and unknown exposure, and the Target-adaptive Importance Mapping module for weighting features based on temporal and spatial relevance. Extensive experiments validate its effectiveness across synthetic and real-world datasets.

## Acknowledgements

This work was supported by Institute of Information & communications Technology Planning & Evaluation (IITP) grant funded by the Korea government (MSIT) (No.RS-2025-25443318, Physically-grounded Intelligence: A Dual Competency Approach to Embodied AGI through Constructing and Reasoning in the Real World). This work was supported by Institute of Information & communications Technology Planning & Evaluation(IITP) grant funded by the Korea government (MSIT) (RS-2023-00237965, Recognition, Action and Interaction Algorithms for Open-world Robot Service). This work was supported by the National Research Foundation of Korea (NRF) grant funded by the Korea government (MSIT) (No. RS-2023-00208506). This work was supported in part by the Samsung Electronics Company Ltd, System LSI Division (IO201210-07984-01).

#### References

- [1] Dawit Mureja Argaw and In So Kweon. Long-term video frame interpolation via feature propagation. In *IEEE/CVF Conference on Computer Vision and Pattern Recognition (CVPR)*, pages 3543–3552, 2022.
- [2] Blain Brown. Cinematography: theory and practice: image making for cinematographers and directors. Taylor & Francis, 2016.
- [3] Kang Chen and Lei Yu. Motion deblur by learning residual from events. *IEEE Transactions on Multimedia (TMM)*, 2024.
- [4] Liangyu Chen, Xiaojie Chu, Xiangyu Zhang, and Jian Sun. Simple baselines for image restoration. In *European conference on computer vision (ECCV)*, pages 17–33, 2022.
- [5] Myungsub Choi, Heewon Kim, Bohyung Han, Ning Xu, and Kyoung Mu Lee. Channel attention is all you need for video frame interpolation. In *AAAI Conference on Artificial Intelligence (AAAI)*, pages 10663–10671, 2020.
- [6] Mengyu Chu, You Xie, Jonas Mayer, Laura Leal-Taixé, and Nils Thuerey. Learning temporal coherence via self-supervision for gan-based video generation. *ACM Transactions on Graphics (TOG)*, 2020.
- [7] Jiong Dong, Kaoru Ota, and Mianxiong Dong. Video frame interpolation: A comprehensive survey. *ACM Transactions on Multimedia Computing, Communications and Applications (TOMM)*, pages 1–31, 2023.

- [8] Guillermo Gallego, Tobi Delbrück, Garrick Orchard, Chiara Bartolozzi, Brian Taba, Andrea Censi, Stefan Leutenegger, Andrew J Davison, Jörg Conradt, Kostas Daniilidis, et al. Event-based vision: A survey. *IEEE Transactions on Pattern Analysis and Machine Intelligence (TPAMI)*, 2020.
- [9] Weihua He, Kaichao You, Zhendong Qiao, Xu Jia, Ziyang Zhang, Wenhui Wang, Huchuan Lu, Yaoyuan Wang, and Jianxing Liao. Timereplayer: Unlocking the potential of event cameras for video interpolation. In *IEEE/CVF Conference on Computer Vision and Pattern Recognition (CVPR)*, pages 17804–17813, 2022.
- [10] Ping Hu, Simon Niklaus, Stan Sclaroff, and Kate Saenko. Many-to-many splatting for efficient video frame interpolation. In *IEEE/CVF Conference on Computer Vision and Pattern Recognition (CVPR)*, pages 3553–3562, 2022.
- [11] Zhewei Huang, Tianyuan Zhang, Wen Heng, Boxin Shi, and Shuchang Zhou. Real-time intermediate flow estimation for video frame interpolation. In *European Conference on Computer Vision (ECCV)*, pages 624–642, 2022.
- [12] Bo Ji and Angela Yao. Multi-scale memory-based video deblurring. In *IEEE/CVF Conference on Computer Vision and Pattern Recognition (CVPR)*, pages 1919–1928, 2022.
- [13] Zhe Jiang, Yu Zhang, Dongqing Zou, Jimmy Ren, Jiancheng Lv, and Yebin Liu. Learning event-based motion deblurring. In *IEEE/CVF Conference on Computer Vision and Pattern Recognition (CVPR)*, pages 3320–3329, 2020.
- [14] Meiguang Jin, Zhe Hu, and Paolo Favaro. Learning to extract flawless slow motion from blurry videos. In *IEEE/CVF Conference on Computer Vision and Pattern Recognition (CVPR)*, pages 8112–8121, 2019.
- [15] Justin Johnson, Alexandre Alahi, and Li Fei-Fei. Perceptual losses for real-time style transfer and super-resolution. In *European Conference on Computer Vision (ECCV)*, pages 694–711, 2016.
- [16] Taewoo Kim, Jeongmin Lee, Lin Wang, and Kuk-Jin Yoon. Event-guided deblurring of unknown exposure time videos. In *European Conference on Computer Vision (ECCV)*, pages 519–538, 2022.
- [17] Lingtong Kong, Boyuan Jiang, Donghao Luo, Wenqing Chu, Xiaoming Huang, Ying Tai, Chengjie Wang, and Jie Yang. Ifrnet: Intermediate feature refine network for efficient frame interpolation. In *IEEE/CVF Conference on Computer Vision and Pattern Recognition (CVPR)*, pages 1969–1978, 2022.
- [18] Hyeongmin Lee, Taeoh Kim, Tae-young Chung, Daehyun Pak, Yuseok Ban, and Sangyoun Lee. Adacof: Adaptive collaboration of flows for video frame interpolation. In *IEEE/CVF Conference on Computer Vision and Pattern Recognition (CVPR)*, pages 5316–5325, 2020.
- [19] Songnan Lin, Jiawei Zhang, Jinshan Pan, Zhe Jiang, Dongqing Zou, Yongtian Wang, Jing Chen, and Jimmy Ren. Learning event-driven video deblurring and interpolation. In *European Conference on Computer Vision (ECCV)*, pages 695–710, 2020.

- [20] Ilya Loshchilov and Frank Hutter. Sgdr: Stochastic gradient descent with warm restarts. *arXiv preprint arXiv:1608.03983*, 2016.
- [21] Ilya Loshchilov and Frank Hutter. Decoupled weight decay regularization. *arXiv* preprint arXiv:1711.05101, 2017.
- [22] Liying Lu, Ruizheng Wu, Huaijia Lin, Jiangbo Lu, and Jiaya Jia. Video frame interpolation with transformer. In *IEEE/CVF Conference on Computer Vision and Pattern Recognition (CVPR)*, pages 3532–3542, 2022.
- [23] Yunfan Lu, Zipeng Wang, Minjie Liu, Hongjian Wang, and Lin Wang. Learning spatial-temporal implicit neural representations for event-guided video super-resolution. In *IEEE/CVF Conference on Computer Vision and Pattern Recognition (CVPR)*, 2023.
- [24] Ana I Maqueda, Antonio Loquercio, Guillermo Gallego, Narciso García, and Davide Scaramuzza. Event-based vision meets deep learning on steering prediction for self-driving cars. In *IEEE/CVF conference on computer vision and pattern recognition* (*CVPR*), pages 5419–5427, 2018.
- [25] Anish Mittal, Rajiv Soundararajan, and Alan C Bovik. Making a "completely blind" image quality analyzer. *IEEE Signal processing letters (SPL)*, 2012.
- [26] Seungjun Nah, Tae Hyun Kim, and Kyoung Mu Lee. Deep multi-scale convolutional neural network for dynamic scene deblurring. In *IEEE Conference on Computer Vision and Pattern Recognition (CVPR)*, pages 3883–3891, 2017.
- [27] Simon Niklaus and Feng Liu. Softmax splatting for video frame interpolation. In *IEEE/CVF Conference on Computer Vision and Pattern Recognition (CVPR)*, pages 5437–5446, 2020.
- [28] Simon Niklaus, Long Mai, and Feng Liu. Video frame interpolation via adaptive convolution. In *IEEE Conference on Computer Vision and Pattern Recognition (CVPR)*, pages 670–679, 2017.
- [29] Liyuan Pan, Cedric Scheerlinck, Xin Yu, Richard Hartley, Miaomiao Liu, and Yuchao Dai. Bringing a blurry frame alive at high frame-rate with an event camera. In *IEEE/CVF Conference on Computer Vision and Pattern Recognition (CVPR)*, pages 6820–6829, 2019.
- [30] Henri Rebecq, Daniel Gehrig, and Davide Scaramuzza. Esim: an open event camera simulator. In *Conference on Robot Learning (CoRL)*, pages 969–982, 2018.
- [31] Fitsum Reda, Janne Kontkanen, Eric Tabellion, Deqing Sun, Caroline Pantofaru, and Brian Curless. Film: Frame interpolation for large motion. In *European Conference on Computer Vision (ECCV)*, pages 250–266, 2022.
- [32] Olaf Ronneberger, Philipp Fischer, and Thomas Brox. U-net: Convolutional networks for biomedical image segmentation. In *International Conference on Medical Image Computing and Computer-Assisted Intervention (MICCAI)*, pages 234–241, 2015.

- [33] Ramprasaath R Selvaraju, Michael Cogswell, Abhishek Das, Ramakrishna Vedantam, Devi Parikh, and Dhruv Batra. Grad-cam: Visual explanations from deep networks via gradient-based localization. In *IEEE/CVF International Conference on Computer Vision (ICCV)*, pages 618–626, 2017.
- [34] Wei Shang, Dongwei Ren, Yi Yang, Hongzhi Zhang, Kede Ma, and Wangmeng Zuo. Joint video multi-frame interpolation and deblurring under unknown exposure time. In *IEEE/CVF Conference on Computer Vision and Pattern Recognition (CVPR)*, pages 13935–13944, 2023.
- [35] Wang Shen, Wenbo Bao, Guangtao Zhai, Li Chen, Xiongkuo Min, and Zhiyong Gao. Blurry video frame interpolation. In *IEEE/CVF Conference on Computer Vision and Pattern Recognition (CVPR)*, pages 5114–5123, 2020.
- [36] Zhihao Shi, Xiaohong Liu, Kangdi Shi, Linhui Dai, and Jun Chen. Video frame interpolation via generalized deformable convolution. *IEEE Transactions on Multimedia* (*TMM*), 24:426–439, 2021.
- [37] Zhihao Shi, Xiangyu Xu, Xiaohong Liu, Jun Chen, and Ming-Hsuan Yang. Video frame interpolation transformer. In *IEEE/CVF Conference on Computer Vision and Pattern Recognition (CVPR)*, pages 17482–17491, 2022.
- [38] Maitreya Suin and AN Rajagopalan. Gated spatio-temporal attention-guided video deblurring. In *IEEE/CVF Conference on Computer Vision and Pattern Recognition* (CVPR), pages 7802–7811, 2021.
- [39] Lei Sun, Christos Sakaridis, Jingyun Liang, Qi Jiang, Kailun Yang, Peng Sun, Yaozu Ye, Kaiwei Wang, and Luc Van Gool. Event-based fusion for motion deblurring with cross-modal attention. In *European Conference on Computer Vision (ECCV)*, pages 412–428, 2022.
- [40] Lei Sun, Christos Sakaridis, Jingyun Liang, Peng Sun, Jiezhang Cao, Kai Zhang, Qi Jiang, Kaiwei Wang, and Luc Van Gool. Event-based frame interpolation with adhoc deblurring. In *IEEE/CVF Conference on Computer Vision and Pattern Recognition* (*CVPR*), pages 18043–18052, 2023.
- [41] Stepan Tulyakov, Daniel Gehrig, Stamatios Georgoulis, Julius Erbach, Mathias Gehrig, Yuanyou Li, and Davide Scaramuzza. Time lens: Event-based video frame interpolation. In *IEEE/CVF Conference on Computer Vision and Pattern Recognition (CVPR)*, pages 16155–16164, 2021.
- [42] Stepan Tulyakov, Alfredo Bochicchio, Daniel Gehrig, Stamatios Georgoulis, Yuanyou Li, and Davide Scaramuzza. Time lens++: Event-based frame interpolation with parametric non-linear flow and multi-scale fusion. In *IEEE/CVF Conference on Computer Vision and Pattern Recognition (CVPR)*, pages 17755–17764, 2022.
- [43] Zhou Wang, Alan C Bovik, Hamid R Sheikh, and Eero P Simoncelli. Image quality assessment: from error visibility to structural similarity. *IEEE Transactions on Image Processing (TIP)*, 2004.

- [44] Wenming Weng, Yueyi Zhang, and Zhiwei Xiong. Event-based blurry frame interpolation under blind exposure. In *IEEE/CVF Conference on Computer Vision and Pattern Recognition (CVPR)*, pages 1588–1598, 2023.
- [45] Zhijian Wu, Jun Li, Chang Xu, Dingjiang Huang, and Steven CH Hoi. Run: Rethinking the unet architecture for efficient image restoration. *IEEE Transactions on Multimedia* (*TMM*), 2024.
- [46] Richard Zhang, Phillip Isola, Alexei A Efros, Eli Shechtman, and Oliver Wang. The unreasonable effectiveness of deep features as a perceptual metric. In *IEEE/CVF Conference on Computer Vision and Pattern Recognition (CVPR)*, pages 586–595, 2018.
- [47] Xiang Zhang and Lei Yu. Unifying motion deblurring and frame interpolation with events. In *IEEE/CVF Conference on Computer Vision and Pattern Recognition* (CVPR), pages 17765–17774, 2022.
- [48] Xiang Zhang, Lei Yu, Wen Yang, Jianzhuang Liu, and Gui-Song Xia. Generalizing event-based motion deblurring in real-world scenarios. In *Proceedings of the IEEE/CVF International Conference on Computer Vision (CVPR)*, pages 10734–10744, 2023.
- [49] Youjian Zhang, Chaoyue Wang, and Dacheng Tao. Video frame interpolation without temporal priors. In *Advances in Neural Information Processing Systems (NeurIPS)*, pages 13308–13318, 2020.

Table S1: tOF↓ / tLP↓ evaluations on GoPro and HighREV with RandEX setting.

tOF↓/tLP↓									
Dataset	Ours	EBFI	REFID	EVDI	UEVD + TL	VIDUE	UTI	NAFnet + RIFE	
GoPro-10 ↓	0.0067 / 0.6366	0.0082 / 0.8873	0.0078 / 0.7618	0.0104 / 0.8324	0.0206 / 1.4478	0.0232 / 1.5676	0.0410 / 3.9124	0.0495 / 4.6272	
GoPro-16 ↓	0.0867 / 0.7618	0.1064 / 0.9227	0.1073 / 0.9827	0.1270 / 1.0581	0.469 / 6.2587	0.337 / 2.8956	0.398 / 4.9081	0.404 / 5.0532	
HighREV-10 ↓	0.0048 / 4.212	0.0064 / 6.522	0.0052 / 5.691	0.0052 / 5.752	0.0094 / 7.231	0.0157 / 8.078	0.0162 / 11.814	0.0158 / 10.584	
HighREV-16 ↓	0.0053 / 4.556	0.0083 / 7.145	0.0059 / 6.170	0.0060 / 6.132	0.0114 / 7.543	0.0158 / 9.072	0.0173 / 11.648	0.0177 / 10.329	

Table S2: NIQE evaluations on RealBlur-DAVIS.

NIQE↓								
Dataset	Ours	EBFI	REFID	EVDI	UEVD + TL	VIDUE	UTI	NAFnet + RIFE
RealBlur-DAVIS	26.55	28.62	29.48	38.97	37.79	36.72	40.67	41.14

In this supplementary material, we first present additional results in Sec. A. Next, we provide network details in Sec. B. Finally, Sec. C discusses the limitations of our approach.

#### A Additional Results

#### A.1 More Quantitative Results

We additionally report temporal consistency metrics (tOF, tLP [1]) and the no-reference quality metric NIQE [23] for RealBlur-DAVIS, which lacks ground-truth frames. As shown in Table S1, our method achieves the most temporally coherent results on both GoPro and HighREV datasets. Furthermore, Table S2 shows that our method also achieves the best NIQE scores, indicating superior perceptual quality on real-world blurry videos.

#### **A.2** More Qualitative Results

We present additional visual comparisons on GoPro, HighREV, and RealBlur-DAVIS in Fig.S4, Fig.S5, Fig.S6, and Fig.S7. On the synthetic GoPro dataset (Fig.S4), our method consistently produces the most faithful results across diverse scenes. For HighREV (Fig.S5), visualizations across various target timestamps show that our method maintains high-quality reconstructions with minimal artifacts.

On the RealBlur-DAVIS dataset (Figs. S6 and S7), two-stage methods (UEVD + TL) yield the least effective results, while event-guided approaches (Ours, EBFI, REFID) outperform the RGB-only baseline (VIDUE) by leveraging precise motion cues from events. Notably, as seen in Fig. S6, event-guided methods can even recover objects missing from RGB frames thanks to the high dynamic range of event sensors. Among them, our method delivers the most reliable results across all target timestamps.

We also provide two types of supplementary MP4 video clips: (1) comparisons with strong baselines (EBFI [12]] and REFID [12]), and (2) demonstrations showing our method upscaling low-frame-rate blurry inputs into sharp, high-frame-rate outputs at arbitrary temporal scales. These videos further highlight the temporal coherence and scalability of our approach.

#### **A.3** More Analysis

We qualitatively ablate the TES module by removing the sampling step and the positional encoding of the target timestamp  $\tau$ . Figure S1 illustrates the resulting changes in channel-wise importance scores. Without sampling (Fig.S1(a)), TES fails to focus on events around

Complexity	Ours	REFID	EBFI	EVDI	UEVD + TL	VIDUE	UTI	NAFnet + RIFE
# Params (M)	10.58	15.76	4.23	0.396	107.09	62.46	49.02	70.07
FLOPs (G)	166.83	182.04	70.08	53.08	671.83	285.93	221.09	189.66
Runtime (ms)	90.93	164.6	96.23	69.2	420.4	195.4	192.3	152.4
PSNR	33.39	31.03	30.89	27.51	23.51	25.86	22.17	21.05

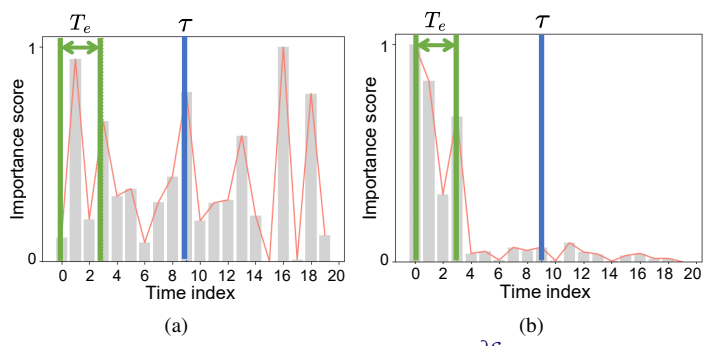


Figure S1: Channel-wise average importance scores  $\frac{\partial \mathcal{E}_{\tau \to [s,t_e]}}{\partial \mathbb{E}_N}$  showing how much each temporal slice in  $\mathbb{E}_N$  contributes to the sampled events. (a) Without the sampling process and (b) without the target timestamp  $\tau$ . Higher scores indicate stronger selection by the TES module.

 $\tau$  and  $T_e$ ; without  $\tau$  (Fig.S1(b)), it only attends to  $T_e$ . These results highlight the critical role of both components in effective event sampling.

To further evaluate the effectiveness of the TIM module, Fig. S2 compares the PSNR over time between our full model and a variant that uses only a single frame and its corresponding events. The results underscore the role of TIM in enhancing temporal consistency across frames.

Computational Cost. Table S3 compares model parameters, FLOPs, and runtime. EVDI [12] has the lowest cost due to its lightweight design, but shows limited performance under unknown and dynamic exposures. EBFI [12] is more efficient than ours in parameters and FLOPs, but lacks temporal modeling, leading to lower performance. Our method, while relatively heavier in parameters and FLOPs, achieves substantially better performance with comparable runtime by leveraging temporal constraints.

# **B** Network Details

Fig. S3 illustrates the detailed architectures of the encoder and decoder, which are not fully described in the main paper. The frame encoder processes the consecutive captured frames, while the event encoder extracts features from the stacked events produced by the TES module. These features are then fused via a channel-wise attention mechanism [5]. The fused representations are adaptively blended by the TIM module to produce the target feature  $\hat{F}_{\tau}$ . The decoder takes  $\hat{F}_{\tau}$  along with the positional encoding of the target timestamp  $\tau$  to reconstruct the sharp target frame  $\hat{I}_{\tau}$ . A final refinement step is applied using the fusion network adopted from [5].

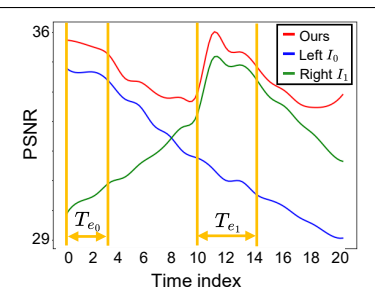


Figure S2: PSNR comparison over time with and without temporal constraints. Our method (red) maintains stable performance across target timestamps, while the version without temporal constraints (blue & green) shows degradation.

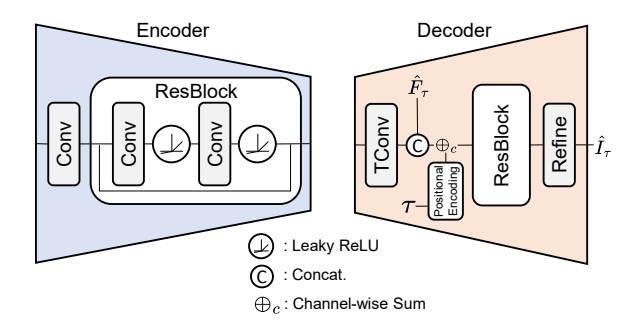


Figure S3: Detailed architecture of the encoder and decoder. Frame and event encoders share the same structure. The model follows a U-Net design with three encoders and two decoders, where only the final decoder includes a refinement block.



Figure S4: Qualitative results on GoPro (synthetic blur & events).



Figure S5: Qualitative results on HighREV (synthetic blur & real events).

#### C Limitation and Future Work

Although we have shown the effectiveness of our method, it has certain limitations that are worth further exploration. Specifically, the current framework assumes that frames and events share the same spatial resolution. In real-world scenarios, however, frame-based cameras and event sensors often operate at different resolutions [N]. To enhance the practicality of our approach, future work could explore strategies for fusing frame and event data with mismatched resolutions. One promising direction is to incorporate implicit neural representations for resolution-agnostic fusion [L], [LN], which we leave as a potential avenue for future research.

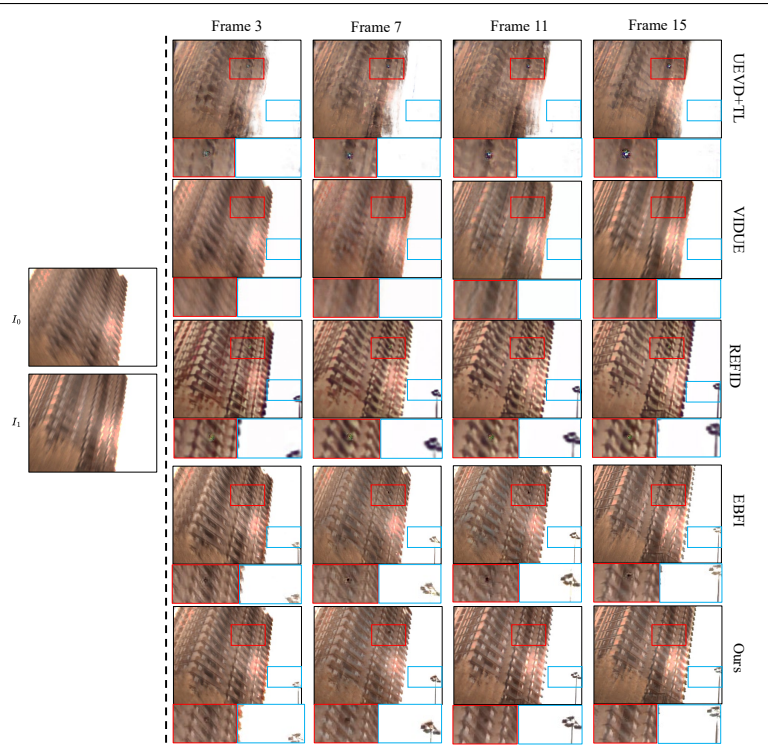


Figure S6: More qualitative results on RealBlur-DAVIS (real blur & events)

Frame 3 Frame 7 Frame 11 Frame 15

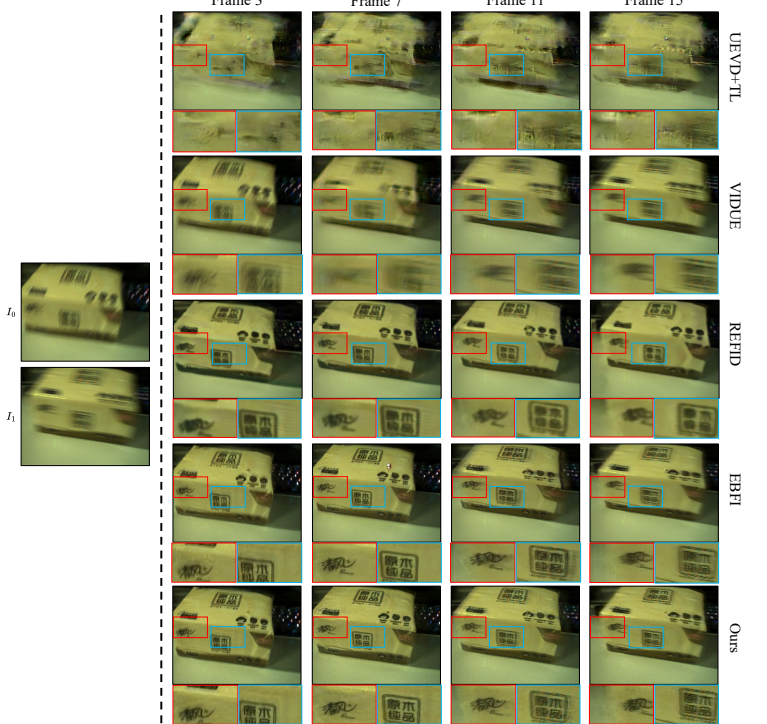


Figure S7: (continued) More qualitative results on RealBlur-DAVIS.